A RESOLVED DEBRIS DISK AROUND THE CANDIDATE PLANET-HOSTING STAR HD95086

A. Moór[1], P. Ábrahám[1], Á. Kóspál[2], Gy. M. Szabó[1,3,4], D. Apai[5], Z. Balog[6], T. Csengeri[7], C. Grady[8,9], Th. Henning[6], A. Juhász[10], Cs. Kiss[1], I. Pascucci[5], J. Szulágyi[11], and R. Vavrek[12]

Draft version September 9, 2013

ABSTRACT

Recently, a new planet candidate was discovered on direct images around the young (10-17 Myr) A-type star HD95086. The strong infrared excess of the system indicates that, similarly to HR8799, β Pic, and Fomalhaut, the star harbors a circumstellar disk. Aiming to study the structure and gas content of the HD95086 disk, and to investigate its possible interaction with the newly discovered planet, here we present new optical, infrared and millimeter observations. We detected no CO emission, excluding the possibility of an evolved gaseous primordial disk. Simple blackbody modeling of the spectral energy distribution suggests the presence of two spatially separate dust belts at radial distances of 6 and 64 AU. Our resolved images obtained with the *Herschel Space Observatory* reveal a characteristic disk size of $\sim 6\rlap{.}''0 \times 5\rlap{.}''4$ (540×490 AU) and disk inclination of $\sim 25°$. Assuming the same inclination for the planet candidate's orbit, its re-projected radial distance from the star is 62 AU, very close to the blackbody radius of the outer cold dust ring. The structure of the planetary system at HD95086 resembles the one around HR8799. Both systems harbor a warm inner dust belt and a broad colder outer disk and giant planet(s) between the two dusty regions. Modelling implies that the candidate planet can dynamically excite the motion of planetesimals even out to 270 AU via their secular perturbation if its orbital eccentricity is larger than about 0.4. Our analysis adds a new example to the three known systems where directly imaged planet(s) and debris disks co-exist.

Subject headings: circumstellar matter — infrared: stars — stars: individual (HD 95086)

1. INTRODUCTION

Recently, several new massive exoplanets at large orbital radii were directly imaged, e.g. around HR8799 (Marois et al. 2008), β Pic (Lagrange et al. 2009), and Fomalhaut (Kalas et al. 2008). They are the largest products of the planet formation process, which also produces many smaller planetesimals. While these smaller bodies cannot directly be detected, *debris* dust arising from their erosion can be observed via scattered light and/or thermal emission of the grains. All three mentioned examples harbor luminous debris disks. Giant planet(s) and the planetesimal belt/debris disk can in-

teract with each other in several ways. A giant planet can sculpt the structure of the debris disk (Ertel et al. 2012), while the planetesimal disk can also influence the planet's orbital evolution and long-term stability (Moore & Quillen 2013).

Rameau et al. (2013) discovered a new planet candidate around HD95086, at a projected separation of 56 AU. Its estimated mass of 4–5 $M_{\rm Jup}$ makes it the lowest mass planet detected by direct imaging. The host star, similarly to HR8799 and β Pic, is an A-type star, belongs to a young association (Lower Centaurus Crux, de Zeeuw et al. 1999, hereafter, LCC), and exhibits prominent infrared excess indicative of a dusty circumstellar disk (Rhee et al. 2007; Chen et al. 2012; Rizzuto et al. 2012). The age estimates of the LCC association range between 10 Myr (Song et al. 2012) and 17 Myr (Pecaut et al. 2012). While the disk of HD95086 probably contains secondary dust, considering its young age, it is possible that the disk is an evolved gaseous primordial disk. Here, we study the structure and gas content of the HD95086 disk and investigate its possible interaction with the newly discovered planet. Our analysis adds a new example to the three known systems where directly imaged planet(s) and debris disks co-exist.

2. OBSERVATIONS AND DATA REDUCTION

We observed HD95086 with the *Herschel Space Observatory* (Pilbratt et al. 2010) using the Photodetector Array Camera and Spectrometer (PACS, Poglitsch et al. 2010), and the Spectral and Photometric Imaging Receiver (SPIRE, Griffin et al. 2010). PACS observations were performed on 2011 August 1 in mini scan map mode with medium scan speed ($20''$ s^{-1}). Measurements at scan angles of $70°$ and $110°$ were made both at $70\,\mu$m and $100\,\mu$m and this setup also provided four observations at

moor@konkoly.hu

[1] Konkoly Observatory, Research Centre for Astronomy and Earth Sciences, Hungarian Academy of Sciences, PO Box 67, H-1525 Budapest, Hungary

[2] European Space Agency (ESA/ESTEC, SRE-SA), P.O. Box 299, 2200 AG, Noordwijk, The Netherlands ; ESA fellow

[3] ELTE Gothard Astrophysical Observatory, Szent Imre herceg út 112, H-9700 Szombathely, Hungary

[4] Dept. of Experimental Physics and Astronomical Observatory, 6720 Szeged Dóm tér 9., Hungary

[5] Department of Astronomy and Department of Planetary Sciences, The University of Arizona, Tucson, AZ 85721

[6] Max-Planck-Institut für Astronomie, Königstuhl 17, 69117 Heidelberg, Germany

[7] Max-Planck-Institut für Radioastronomie, Auf dem Hügel 69, 53121 Bonn, Germany

[8] NASA Goddard Space Flight Center, Code 667, Greenbelt, MD 20771, USA

[9] Eureka Scientific, 2452 Delmer Street, Suite 100, Oakland, CA 94602, USA

[10] Leiden Observatory, Leiden University, Niels Bohrweg 2, NL-2333 CA Leiden, The Netherlands

[11] Université de Nice Sophia-Antipolis, Observatoire de la Côte d'Azur, CNRS UMR 7293, 06108, Nice Cedex 2, France

[12] Herschel Science Centre, ESA/ESAC, PO Box 78, Villanueva de la Cañada, 28691, Madrid, Spain

$160\,\mu$m. Each measurement included four repetitive scan maps. Data pocessing was carried out with the Herschel Interactive Processing Environment (HIPE, Ott 2010), v.9.2, using the pipeline optimized for bright sources. 1/f noise was removed by highpass filtering, after our target was masked to avoid flux loss. We used second-level deglitching to remove glitches. Mosaics (Fig. 1) were created with pixel sizes of $1\rlap{.}''1$, $1\rlap{.}''4$, and $2\rlap{.}''1$ at 70, 100, and 160 μm, by combining the individual scan maps with a weighted average. SPIRE maps were obtained on 2011 August 16 at 250, 350 and 500 μm in small scan map mode with a repetition factor of 2. Data reduction was performed with HIPE v9.2 using the standard pipeline script. The beam size was $18\rlap{.}''1$, $25\rlap{.}''2$ and $36\rlap{.}''6$ at 250, 350, and 500 μm, respectively, and the maps were resampled to pixel sizes of $6''$, $10''$, and $14''$.

HD95086 was observed with the InfraRed Spectrograph (IRS) onboard the *Spitzer Space Telescope* on 2004 February 4. Small 2×3 maps were taken using the low-resolution IRS modules, covering the $5.2 - 38\,\mu$m wavelength range with a spectral resolution of $R = 60 - 120$. We downloaded the data processed with the pipeline version S18.18.0 from the archive and further processed them with the Spitzer IRS Custom Extraction Software (SPICE v2.5.0). We treated the data as a nodding measurement by using the two central map positions and subtracting them from each other. Then, we extracted the positive signal from a wavelength-dependent, tapered aperture, and averaged them. The final spectrum is plotted in Fig. 2a.

On 2011 April 22, we observed HD95086 at the 345.796 GHz ^{12}CO $J{=}3{-}2$ line using the SHeFI/APEX2 receiver (Vassilev et al. 2008) mounted at the 12 m APEX telescope[13] (Güsten et al. 2006) (M-087.F-0001 program, PI: Th. Henning). We used the Fast Fourier Transform Spectrometer with 2048 channels, providing a velocity resolution of $0.42\,\mathrm{km\,s^{-1}}$. An on-off observing pattern was utilized with beam switching. The total on-source integration time was 29.4 minutes. The data reduction was performed using GILDAS/CLASS[14]. For the final spectrum, we subtracted a linear baseline from each individual scan, and averaged them after omitting the noisy scans.

We obtained a high-resolution optical spectrum of HD95086 with the Fiber-fed Extended Range Optical Spectrograph (FEROS, Kaufer et al. 1999) mounted at the 2.2 m MPG/ESO telescope in La Silla, Chile, on 2011 April 17. This instrument covers the wavelength range between 3500 and 9200 Å in 39 echelle orders with a resolution of $R \approx 48\,000$. We used the "object-sky" mode, with one fiber positioned at the target, and the other one on the sky. The integration time was 120 s. Data reduction, including bias subtraction, flat-field correction, background subtraction, the definition and extraction of orders, and wavelength calibration, was performed using the FEROS data reduction system pipeline at the telescope.

3. RESULTS AND ANALYSIS

3.1. *Stellar properties*

To estimate the basic properties of HD95086 and provide photospheric flux predictions at relevant mid- and far-IR wavelengths, we modeled the stellar photosphere by fitting the optical and infrared photometric data with an ATLAS9 atmosphere model (Castelli & Kurucz 2003). We used photometry from *Hipparcos* (Perryman et al. 1997), *TYCHO2* (Høg et al. 2000), and 2MASS (Skrutskie et al. 2006) that were supplemented by $W1$ band (centered on $3.4\,\mu$m) photometry from *WISE* (Wright et al. 2010). Assuming that the interstellar reddening is negligible and adopting solar metallicity and $\log g = 4.0$, our χ^2 minimization yielded $T_{\mathrm{eff}} = 7500{\pm}150\,$K and a luminosity of $L_{\mathrm{bol}} = 7.0{\pm}0.6\,\mathrm{L_\odot}$ (using a *Hipparcos*-based distance of 90.4 pc, van Leeuwen 2007). The derived T_{eff} is identical with that obtained by Chen et al. (2012) from color indices.

To obtain T_{eff}, $\log g$, and $v\sin i$ from our FEROS spectrum, we used an iterative fitting method described in e.g. Szabó et al. (2011). First, we varied these three parameters using spectra from Munari et al. (2005), in the 4000–6200Å wavelength range, excluding the H_β region and Na D lines. Radial velocity was calculated from the cross-correlation function, convolving the measured spectrum with the best-fit Munari template, but setting $\log g$ to 1.0 and $v\sin i$ to 0. This yielded $17{\pm}2\,\mathrm{km\,s^{-1}}$. After transforming the measured spectrum to the laboratory system, and keeping T_{eff}, $\log g$, and $v\sin i$ in the global minimum, we fitted [Fe/H] in the second step. T_{eff} and $\log g$ was re-fitted in the third iteration. Our best-fit parameters are $T_{\mathrm{eff}} = 7750 \pm 250$K, $\log g = 4.0 \pm 0.5$, $v\sin i = 20 \pm 10\mathrm{kms^{-1}}$, [Fe/H] $= -0.25{\pm}0.5$. This T_{eff} supports our result obtained from the photometry (see above). Rameau et al. (2013) estimated a stellar mass of 1.6 $\mathrm{M_\odot}$ for HD95086.

3.2. *Herschel maps*

HD95086 appeared as an isolated bright source on our PACS images (Fig. 1, upper panels). To estimate the disk size, we constructed point spread functions (PSFs) using PACS observations of two calibrator stars (α Boo, α Tau) without known infrared excess, measured and processed in the same way as HD95086. The PSF maps were rotated to match the roll angle of the telescope at the time of observing HD95086. The FWHM point-source sizes, as measured on these maps are $5\rlap{.}''5{\pm}0\rlap{.}''1$, $6\rlap{.}''7{\pm}0\rlap{.}''1$, and $10\rlap{.}''6{\pm}0\rlap{.}''3$ at 70, 100, and 160μm, respectively. We derived azimuthally averaged radial brightness profiles and averaged the individual measurements to obtain a reference PSF. By comparing the azimuthally averaged radial brightness profiles of HD95086 with these reference PSFs, we found that the disk around HD95086 is spatially extended at all PACS wavelengths (Fig. 1, lower panels).

We fitted elliptical Gaussians to the images of the source in order to derive the FWHM sizes of the major and minor axes and the position angles (see Table 1). Then, we estimated the disk size by quadratic deconvolution with the PSF, and calculated the inclination (at 70 and 100μm) assuming that the intrinsic shape/structure of the disk is azimuthally symmetric. The contribution of stellar photosphere to the total flux was negligible ($<0.3\%$) in all bands, thus we did not subtract
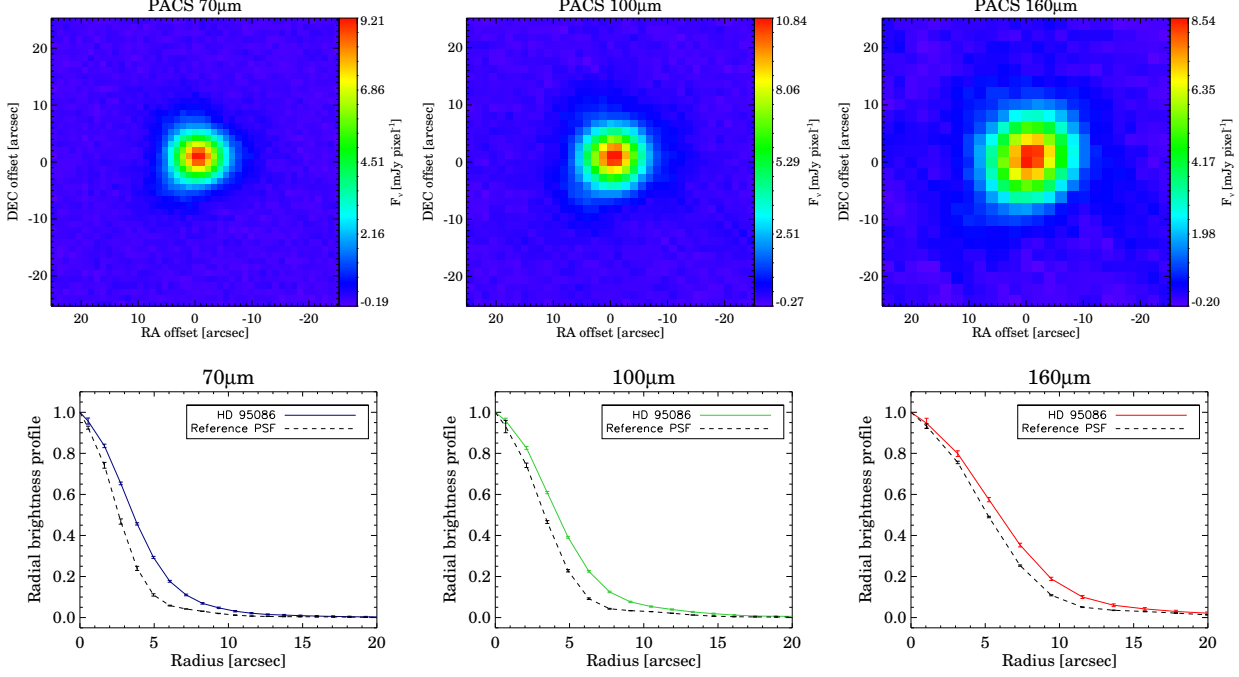
Figure 1. *Upper: Herschel PACS 70/100/160μm images of HD95086. Lower: radial brightness profiles for HD95086 and reference PSF profiles at the same wavelengths (see Sect. 3.2).*

the model photospheric emissions from the source images before the Gaussian fitting. Table 1 lists the final parameters and their uncertainties. The coarse spatial resolution at 160 μm prevented us from determining a reliable position angle and inclination. Our results outline a large disk with a characteristic size of $\sim 6{\farcs}0 \times 5{\farcs}4$ ($\sim 540 \times 490$ AU).

We measured the flux of HD95086 on the individual PACS scan maps using an aperture radius of $18''$ and a sky annulus between $40''$ and $50''$. We calculated the average and RMS of the individual flux values, applied aperture correction, and calculated the final uncertainties of the photometry by adding quadratically the measurement errors and an absolute calibration uncertainty of 7% (Balog et al., submitted). Our target was clearly detected as a point source at all SPIRE wavelengths. We performed photometry with an aperture radius of $22''$, $30''$, and $42''$ at 250, 350, and 500 μm. Background levels were estimated in annuli extending from $60''$ to $90''$. The final uncertainties were derived as the quadratic sum of the measurement errors and the overall calibration uncertainty of 5.5% for the SPIRE photometer (Bendo et al. 2013). Our Herschel photometry for HD95086 is listed in Table 2.

3.3. *Modeling of dust distribution*

We compiled the spectral energy distribution (SED) of HD95086 by combining the new PACS and SPIRE fluxes with infrared photometry from the literature. For the fitting process the IRS spectrum was sampled in 11 bins. Table 2 summarizes the collected IR data. The resulting SED with the stellar photosphere model (Sect. 3.1) is presented in Fig. 2a. The IRS spectrum shows that IR excess is present even at $\sim 10\mu$m. No silicate features are apparent, implying the depletion of

small grains. We assumed optically thin dust emission in the modeling, and as a first simple model, we fitted the excess by a single temperature modified blackbody, where the emissivity is equal to 1 at $\lambda \leq \lambda_0$ and varies as $(\lambda/\lambda_0)^{-\beta}$ at $\lambda > \lambda_0$. Following Williams & Andrews (2006), we adopted $\lambda_0 = 100\mu$m. We used a Levenberg-Marquardt algorithm in the modeling, and utilized an iterative method to compute color corrections (Moór et al. 2006). Table 3 lists the best-fit parameters and the reduced χ_r^2 of the fitting. Fig. 2a shows that the best-fit model underestimates the observed excess, especially at shorter wavelengths. This discrepancy can be explained if the emitting dust grains – similarly to many other debris systems (e.g. Morales et al. 2011) and our Solar System – are distributed in two spatially separated rings. With this assumption, we used a two-component model, where grains in the warmer component act like blackbodies, while the emission of the outer ring is described by the modified blackbody as defined above. As Fig. 2a and the improved χ_r^2 value (Table 3) indicate, this model fits the SED better over the whole studied wavelength range. The fractional luminosity of the rings was computed as $f_{\rm dust} = L_{\rm dust}/L_{\rm bol}$. The radius of the dust ring(s) was estimated using the following formula (Backman & Paresce 1993):

$$\frac{r_{\rm dust}}{AU} = \left(\frac{L_{\rm bol}}{L_\odot}\right)^{0.5} \left(\frac{278\,K}{T_{\rm dust}}\right)^2. \qquad (1)$$

Because of the blackbody assumption, the resulting $r_{\rm dust}$ values are lower limits The obtained fundamental disk properties are listed in Table 3.

The dust mass of the disk was estimated using the

Table 1
Disk properties derived from quadratic deconvolution (see Sect 3.2)

	Original FWHM of the source before deconvolution major×minor axis [″]	Disk size after quadratic deconvolution major×minor axis [″]	major×minor axis [AU]	Position angle [°]	Incl. [°]
PACS 70μm	8.1±0.1×7.7±0.1	5.9±0.1×5.4±0.2	∼530×490	99±5	23±5
PACS 100μm	9.1±0.1×8.6±0.1	6.2±0.2×5.4±0.2	∼560×490	113±7	29±4
PACS 160μm	12.5±0.5×12.2±0.4	6.7±1.0×6.1±0.9	∼600×550	...	...

Table 2
Measured and predicted fluxes

Wavelength [μm]	Measured flux density [mJy]	Instrument	Predicted photospheric flux density [mJy]	Reference
3.35	626.7±24.7	WISE	592.3	Wright et al. (2010)
4.60	336.8±11.5	WISE	329.4	Wright et al. (2010)
9.03	95.7±13.0	IRS	90.7	this work
11.02	67.3±7.0	IRS	61.3	this work
11.56	62.7±3.0	WISE	55.8	Wright et al. (2010)
13.02	51.2±5.4	IRS	44.2	this work
14.87	44.7±4.6	IRS	34.0	this work
16.99	40.0±4.4	IRS	26.1	this work
19.02	43.1±5.0	IRS	20.9	this work
21.31	46.7±7.3	IRS	16.7	this work
22.09	51.6±3.3	WISE	15.5	Wright et al. (2010)
23.67	45.6±2.0	MIPS	13.5	Chen et al. (2012)
24.48	59.0±6.0	IRS	12.6	this work
27.45	77.3±7.6	IRS	10.1	this work
30.50	96.7±10.0	IRS	8.1	this work
33.55	137.9±18.6	IRS	6.7	this work
60.00*	601.0±48.1	IRAS	2.1	Moshir et al. (1989)
70.00*	690.1±48.6	PACS	1.5	this work
71.42	655.0±44.4	MIPS	1.5	Chen et al. (2012)
100.00*	675.1±47.6	PACS	0.7	this work
160.00*	462.4±32.7	PACS	0.28	this work
250.00	213.4±12.9	SPIRE	0.12	this work
350.00	120.3±8.7	SPIRE	0.06	this work
500.00	63.6±10.2	SPIRE	0.03	this work

* The emission is spatially resolved at these wavelengths.

Table 3
Disk properties derived from SED fitting

	Single temperature	Two temperature Warm comp.	Cold comp.
χ_r^2	4.6	0.9	
$T_{\rm dust}$ [K]	64±1	187±26	57±1.5
β	0.17±0.06	0	0.41±0.07
$r_{\rm dust}$ [AU]	50±2.4	5.9±1.6	63.7±4.4
$f_{\rm dust}$ [10^{-3}]	1.5±0.1	0.14±0.10	1.4±0.2

following formula:

$$M_{dust} = \frac{F_\nu d^2}{B_\nu(T_{dust})\kappa_\nu}, \qquad (2)$$

where F_ν is the measured SPIRE flux at 500μm, d is the distance to the source (90.4 pc), $\kappa_\nu = \kappa_0(\frac{\nu}{\nu_0})^\beta$ is the mass absorption coefficient, $B_\nu = \frac{2\nu^2 kT_{dust}}{c^2}$ is the Planck function using the Rayleigh-Jeans approximation. Assuming a $\kappa_0 = 2\,{\rm cm}^2\,{\rm g}^{-1}$ at $\nu_0 = 345$ GHz (e.g. Nilsson et al. 2010) and taking $\beta = 0.41$ and $T_{dust} = 57$ K from Table 3, we derived a dust mass of 0.5±0.1 M$_\oplus$.

3.4. CO data

No CO emission was detected in our APEX spectrum. We converted antenna temperatures to flux densities using conversion factors from the APEX web page[15] and computed an upper limit for the CO(3–2) line flux $(S_{CO(3-2)})$ as $I_{\rm rms}\Delta v\sqrt{N}$, where $I_{\rm rms}$=0.95 Jy is the measured RMS noise at the systemic velocity of the star, Δv=0.42 km s^{-1} is the velocity channel width, and N is the number of velocity channels over an interval of 10 km s^{-1}, which covers the expected line width. The resulting upper limit is 1.95 Jy km s^{-1} for $S_{CO(3-2)}$. Assuming optically thin emission and using a range of excitation temperatures between 20 K and 60 K (the latter value corresponds to the dust temperature in the outer ring, see Sect. 3.3), the upper limit for the total CO mass is between 1.4×10^{-4} and 1.7×10^{-4} M$_\oplus$.

4. DISCUSSION

Analyzing *Hipparcos* astrometric data, de Zeeuw et al. (1999) identified a total of 180 probable members in the LCC association. Among their proposed members, HD95086 has the lowest membership probabil-

[15] http://www.apex-telescope.org/telescope/efficiency/

ity of 41%. In order to re-check the membership status of HD95086, we used our new radial velocity and *Hipparcos* astrometric data to compute a Galactic space motion of U = −10.5±1.0, V = −22.3±1.8, W = −5.2±0.4 km s⁻¹. According to Chen et al. (2011), the characteristic space motion of LCC is U = −7.8±0.5, V = −20.7±0.6, W = −6.0±0.3 km s⁻¹, thus there is a good kinematic match between our target and LCC. The position of HD95086 in the color-magnitude diagram in Fig. 2b fits well to the locus defined by LCC members, indicating that its isochrone age is consistent with that of the cluster. Based on these findings, we propose that HD95086 is a very probable member of LCC. With its distance of 90.4 pc, HD95086 is one of the closest member of the association.

Pecaut et al. (2012) derived an age of 17 Myr for LCC based on isochrone fitting while Song et al. (2012) proposed 10 Myr from lithium content of late-type LCC stars. The latter estimate is close to the timescale on which primordial gas is believed to disappear (e.g. Mamajek 2009). Thus, if the 10 Myr age estimate proves to be true, we cannot exclude that this disk would contain substantial amount of primordial gas similarly to transitional disks. Converting our upper limit on the CO mass to total gas mass assuming a canonical H_2/CO abundance ratio of 10^4, the estimated gas mass in the disk of HD95086 is $\lesssim 0.12$ $M_\oplus$ ($\lesssim 3.7 \times 10^{-6}$ $M_\odot$). This is several orders of magnitude below the typical Herbig Ae and transitional disk masses. This result and the low gas-to-dust mass ratio of $\lesssim 0.25$ implies that HD95086 harbors a gas-poor debris disk.

The debris disk of HD95086 has a high fractional luminosity of 1.5×10^{-3}. With this value, it belongs to the top ten highest fractional luminosity debris systems in the solar neighbourhood (d < 120 pc, Moór et al. 2006; Rhee et al. 2007). Interestingly, these systems have other common properties: they are younger than 100 Myr, and most of them belong to different young moving groups and associations. We found that the HD95086 disk contains two dust belts: a warm one with a characteristic temperature of 187 K, and a colder one with 57 K. Such structures seem to be relatively common. Morales et al. (2011) found that a significant fraction of debris disks harbors two spatially distinct dust components. The characteristic dust temperatures for the inner and outer dust belts (190 K and 60 K) were found to be very similar independently of the host stars' luminosity, implying that the formation of dust belts is controlled by a temperature-sensitive mechanism. Several other members of the young massive debris disk group also share similar properties (e.g., Su et al. 2009; Roberge et al. 2013; Donaldson et al. 2013). Because the characteristic temperature of the warm component is slightly above the ice evaporation temperature, Morales et al. (2011) proposed that the formation of the warm component is related to sublimation of icy planetesimals crossing the snow line, or due to collisions in an asteroid belt-like system formed just interior to the snow line (see also Martin & Livio 2013). One of these mechanisms could also work in the case of HD95086.

To determine the relative location of the two dust belts and the planet candidate, we need to constrain the inclination of the planetary orbit. From our resolved Herschel observations, the disk inclination is ∼25°. The star's equatorial plane is probably not very different from this, because the observed $v \sin i = 20$ km s⁻¹ is unusually low compared to stars with similar masses (Zorec & Royer 2012), implying a low stellar inclination. Assuming that the disk and the planet's orbit are coplanar, and taking the projected orbital radius of 56 AU from Rameau et al. (2013), the deprojected orbital radius would be 62 AU. We derived a radius of 64 AU for the outer dust belt. Since we adopted blackbody grains, this is a lower limit, because smaller grains with the same temperature can be located farther from the star. Thus, it is possible that the planet candidate is situated just inside the cold outer dust belt. Further monitoring of the planet candidate will reveal whether it orbits within the outer dust belt. If it stays inside, it might sculpt the inner edge of the belt, and may induce azimuthal asymmetries in the dust distribution. We note that the planetary system of HD95086 resembles the one around HR8799. Both systems harbor a warm inner dust belt and a broad colder outer disk and giant planet(s) between the two dusty regions.

The short lived dust grains in debris disks are believed to be replenished by collisions between larger bodies. For destructive collisions, the collision velocity must exceed a critical value and it requires a dynamical perturbing force. According to theory, this perturbation is linked to 1000 km-sized planetesimals formed within the planetesimal ring (self-stirring, Kenyon & Bromley 2008), or the presence of planet(s) in the system (planetary stirring, Mustill & Wyatt 2009). The formation of 1000 km-sized planetesimals is a slow process at large orbital radii. Adopting an age of 17 Myr for the system and using Eqs. 27,41 from Kenyon & Bromley (2008), we found that, even in a disk with an unusually high initial surface density (ten times higher than the minimum-mass solar nebula), the formation of such large bodies is limited to $\lesssim 70$ AU. Our PACS images show that the disk around HD95086 is spatially extended with a diameter of 540 AU. While large dust grains have the same spatial distribution as the parent planetesimals, the distribution of small grains (smaller than the blowout limit of ∼1.8μm, estimated following Wyatt 2008) can be more extended, because they are expelled by stellar radiation pressure and form a dust halo. However, the contribution of such small grains to the 100 and 160μm flux is small, suggesting that HD95086 harbors an extended planetesimal belt whose dynamical stirring cannot be explained by self-stirring. Mustill & Wyatt (2009) claim that planetary stirring can be faster than self-stirring in the outer regions of planetary systems. Using their formulae, we found that the candidate planet can dynamically excite the motion of planetesimals even at 270 AU via their secular perturbation if its orbital eccentricity is larger than ≈0.4. Alternatively, without effective stirring, collisions with low velocity can lead to merging grains, thus we cannot exclude that the outer disk region contains primordial dust as well.
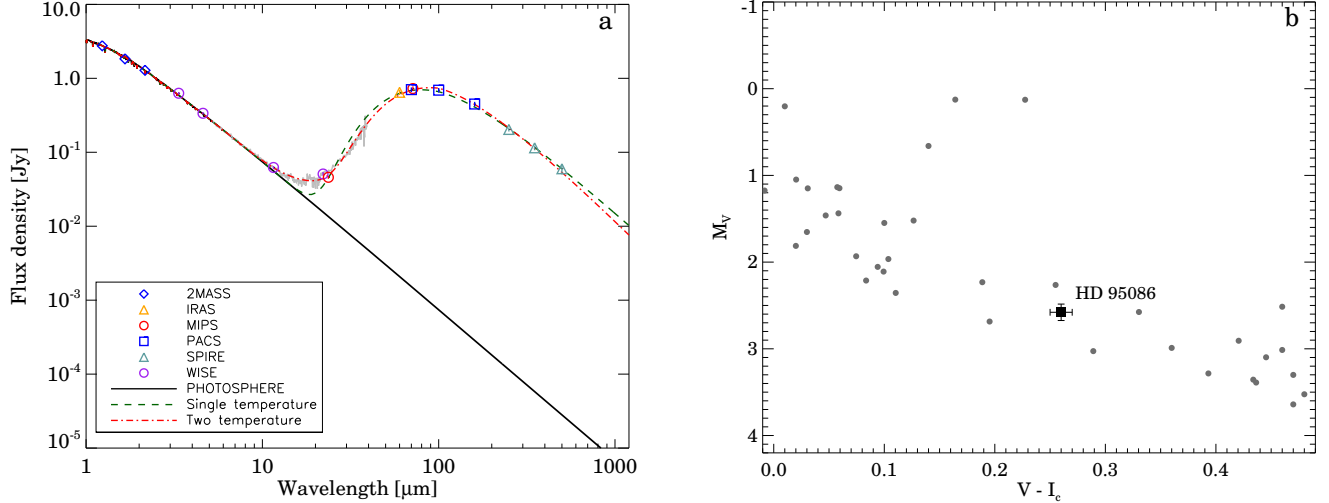
Figure 2. *Left: Color-corrected SED of the source and fitted models. Right: Absolute V band magnitude versus V−I$_c$ color diagram for known members of LCC with parallax error <10% (gray dots) and for HD95086 (black square). Photometric data were taken from the Hipparcos catalog and dereddened using extinction values from Chen et al. (2011, 2012).*

REFERENCES

Backman, D. E., & Paresce, F. 1993, in Protostars and Planets III, ed. E. H. Levy & J. I. Lunine (Tucson: Univ. Arizona Press), 1253

Bendo, G. J., Griffin, M. J., Bock, J. J., et al. 2013, MNRAS, 1713

Castelli, F. & Kurucz, R. L. 2003, Modelling of Stellar Atmospheres (IAU Symp. 210), ed. N. E. Piskunov, W. W. Weiss, & D. F. Gray (San Francisco, CA: ASP), A20

Chen, C. H., Mamajek, E. E., Bitner, M. A., et al. 2011, ApJ, 738, 122

Chen, C. H., Pecaut, M., Mamajek, E. E., Su, K. Y. L., & Bitner, M. 2012, ApJ, 756, 133

de Zeeuw, P. T., Hoogerwerf, R., de Bruijne, J. H. J., Brown, A. G. A., & Blaauw, A. 1999, AJ, 117, 354

Donaldson, J. K., Lebreton, J., Roberge, A., Augereau, J.-C., & Krivov, A. V. 2013, arXiv:1305.7230

Ertel, S., Wolf, S., & Rodmann, J. 2012, A&A, 544, A61

Griffin, M. J., Abergel, A., Abreu, A., et al. 2010, A&A, 518, L3

Güsten, R., Nyman, L. Å., Schilke, P., Menten, K., Cesarsky, C., & Booth, R. 2006, A&A, 454, L13

Høg, E., Fabricius, C., Makarov, V. V., et al. 2000, A&A, 355, L27

Hughes, A. M., Wilner, D. J., Andrews, S. M., et al. 2011, ApJ, 740, 38

Kalas, P., Graham, J. R., Chiang, E., et al. 2008, Science, 322, 1345

Kaufer, A., Stahl, O., Tubbesing, S., et al. 1999, The Messenger, 95, 8

Kenyon, S. J., & Bromley, B. C. 2008, ApJS, 179, 451

Krivov, A. V., Herrmann, F., Brandeker, A., & Thébault, P. 2009, A&A, 507, 1503

Lagrange, A.-M., Kasper, M., Boccaletti, A., et al. 2009, A&A, 506, 927

Mamajek, E. E. 2009, American Institute of Physics Conference Series, 1158, 3

Marois, C., Macintosh, B., Barman, T., et al. 2008, Science, 322, 1348

Martin, R. G., & Livio, M. 2013, MNRAS, 428, L11

Moór, A., Ábrahám, P., Derekas, A., et al. 2006, ApJ, 644, 525

Moór, A., Ábrahám, P., Juhász, A., et al. 2011, ApJ, 740, L7

Moór, A., et al. 2011, ApJS, 193, 4

Morales, F. Y., Rieke, G. H., Werner, M. W., et al. 2011, ApJ, 730, L29

Moshir, M., et al. 1989, Explanatory Supplement to the IRAS Faint Source Survey (Pasadena: JPL) (FSC)

Munari, U., Sordo, R., Castelli, F., & Zwitter, T. 2005, A&A, 442, 1127

Mustill, A. J., & Wyatt, M. C. 2009, MNRAS, 399, 1403

Nilsson, R., et al. 2010, A&A, 518, A40

Ott, S. 2010, Astronomical Data Analysis Software and Systems XIX, 434, 139

Pecaut, M. J., Mamajek, E. E., & Bubar, E. J. 2012, ApJ, 746, 154

Perryman, M. A. C., Lindegren, L., Kovalevsky, J., et al. 1997, A&A, 323, L49

Pilbratt, G. L., Riedinger, J. R., Passvogel, T., et al. 2010, A&A, 518, L1

Poglitsch, A., Waelkens, C., Geis, N., et al. 2010, A&A, 518, L2

Moore, A., & Quillen, A. C. 2013, MNRAS, 430, 320

Rameau, J., Chauvin, G., Lagrange, A.-M., et al. 2013, ApJ, 772, L15

Rhee, J. H., Song, I., Zuckerman, B., & McElwain, M. 2007, ApJ, 660, 1556

Rizzuto, A. C., Ireland, M. J., & Zucker, D. B. 2012, MNRAS, 421, L97

Roberge, A., Kamp, I., Montesinos, B., et al. 2013, ApJ, 771, 69

Siess, L., Dufour, E., & Forestini, M. 2000, A&A, 358, 593

Skrutskie, M. F., Cutri, R. M., Stiening, R., et al. 2006, AJ, 131, 1163

Song, I., Zuckerman, B., & Bessell, M. S. 2012, AJ, 144, 8

Su, K. Y. L., Rieke, G. H., Stapelfeldt, K. R., et al. 2009, ApJ, 705, 314

Szabó, G. M., Szabó, R., Benkő, J. M., et al. 2011, ApJ, 736, L4

van Leeuwen, F. 2007, Astrophysics and Space Science Library, 350, *Hipparcos*, The New Reduction of the Raw Data (Dordrecht: Springer)

Vassilev, V., Meledin, D., Lapkin, I., et al. 2008, A&A, 490, 1157

Williams, J. P., & Andrews, S. M. 2006, ApJ, 653, 1480

Wright, E. L., et al. 2010, AJ, 140, 1868

Wyatt, M. C. 2008, ARA&A, 46, 339

Zorec, J., & Royer, F. 2012, A&A, 537, A120